RSC Advances

ROYAL SOCIETY OF CHEMISTRY

www.rsc.org/advances

Journal Name

ARTICLE

β-$NaGdF_4$:Eu^{3+} nanocrystal markers for melanoma tumor imaging

B. Sojka,[a] A. Podhorodecki,[a] M. Banski,[a] J. Misiewicz,[a] S. Drobczynski,[b] T. Dumych,[c] M. M. Lutsyk,[c] A. Lutsyk[c] and R. Bilyy [c]

Received 00th January 20xx,
Accepted 00th January 20xx

DOI: 10.1039/x0xx00000x

www.rsc.org/

In the current paper, the strategy of tuning optical and structural properties of Eu doped nanocrystals (NCs) is described with the emphasis on obtaining NCs with high brightness and photostability at the desired excitation and emission range. Those NCs are further chemically functionalized and covalently conjugated with lectins, providing specific (but reversible) targeting of pathological glycans on the surface of melanoma cells. Nanoconjugates are then injected intravenously into the blood stream of laboratory mice. Subsequently, histological slices were examined by fluorescent microscopy, whereas whole melanoma tumor by ex vivo fluorescence imaging. Analysis revealed specific targeting, high intensity and photostability of the signal during visualization.

1 Introduction

Recently, a significant development in medical tools and probes for diagnostic purposes have been observed. This is especially true for detection of various cancer types for better and more efficient treatment. However, to improve the quality of these diagnostic tools the probes themselves must fulfil several criteria. The probes should be multifunctional, optically active in near-IR (NIR), non-toxic, biodegradable, bright and optically stable (no blinking and bleaching), small in size and most importantly functionalized with selective vectors (proteins, antibodies, DNA,…) which enable them to target and label cancer cells selectively. Recently used molecular markers, including organic dyes, fluorescent proteins (like Green Fluorescent Protein - GFP) or chelates containing lanthanide ions, have several significant limitations. One of the alternatives for molecular markers are inorganic quantum dots (QDs) (i.e. CdSe, CdS), which are commonly used in many academic works. However, most of the QDs available these days are based on Cd atoms (CdS, CdSe,…), which makes them potentially toxic[1–3] (even chemically), not to mention other side effects related to aggregation of QDs in the body. Thus, reduction of nanoparticle toxicity, no matter which effect is responsible for it, is essential in order to use them in medicine and biology and move with these probes to clinical use. Moreover, it is difficult to fulfil all demands listed above for QDs, especially making them active in NIR or growing them as multimodal probes. On the other hand, there are already several reports[4–15] showing that fluoride ($NaYF_4$, $NaGdF_4$,…) nanocrystals (NCs) doped with rare earth ions (RENCs) can be more suitable candidates for design of better diagnostic probes, with no evidence of biotoxicity so far [16–18]. In addition, these nanocrystals are characterized with no-blinking[19], no bleaching[20], narrow emission lines (< 10 nm) and long emission decay times (~100 ns – 10 ms)[24] and lastly, their emission can be easily tuned spectrally from ultra violet (UV) to infrared (IR) making them either down-shifting or up-converting markers[21–23]. Moreover, and this is important, they can be designed as the multimodal probes (Up-conversion –UPC, Magnetic Resonance Imaging – MRI, Computed Tomography – CT,…)[4–15]. Thus, the absence of biotoxicity and unique optical properties make RENCs very promising candidates for clinical use as diagnostic probes.

However, this potential has been mainly explored for the up-converting fluorides like $NaGdF_4$:Er^{3+}, Yb^{3+} or $NaGdF_4$:Tm^{3+}, Yb^{3+}, for which up-conversion emission in visible spectral range (VIS) is obtained upon 980 nm excitation. For these nanocrystals, it has been shown already that they can be used as probes for optical imaging combined with X-ray CT[25–27], MRI[5,11,28–30], single-photon emission computed tomography (SPECT) or positron emission tomography (PET) imaging[20,31,32]. It should be noted that the main limitation for these nanocrystals is their low emission quantum yield (usually below 1 %), which is highly reduced for nanocrystals smaller than 10 nm, which size is desired for a number of practical applications in biology and medicine[33]. Thus, for these reasons introducing these up-converting nanocrystals into clinical use is still very challenging.

In this paper, as an alternative for up-converting fluoride nanocrystals, the authors report on europium doped, highly emissive fluoride nanocrystals, with excellent imaging

[a] Department of Experimental Physics, Wroclaw University of Technology, Wybrzeze Wyspianskiego 27, 50-370, Wroclaw, Poland
[b] Department of Optics and Photonics, Wroclaw University of Technology, Wybrzeze Wyspianskiego 27, 50-370, Wroclaw, Poland
[c] Danylo Halytsky Lviv National Medical University, 79010, Pekarska Str.69, Lviv, Ukraine

Electronic Supplementary Information (ESI) available: [details of any supplementary information available should be included here]. See DOI: 10.1039/x0xx00000x

potential for a specific kind of tumor, namely melanoma tumor.

The melanomas are considered as one of the most aggressive and fast growing human tumors, and are characterized by high risk of metastasis and death. Since no effective systemic therapy exists to cure melanoma at an advanced stage, surgical removal of thin early stage melanoma remains the best solution for a recovery. Due to its high metastatic potential, a precise visualization of tumor contours during surgical incision or radio therapy is important to ensure and control its complete removal and preserve unaffected (healthy) tissue[34,35]. So far there have been no markers available that would provide in vivo visualization of the tumor due to their intracellular accumulation[36] and low signal-to-noise ratio of the available labels for imaging tissues. Since melanoma is usually localized superficially, its imaging with optical methods is considered the most promising one.

Because there is not a single protein marker of melanoma known on its surface, which could be used to target the tumor, the glycan compositions of melanoma tumors were recently analysed[15]. Glycan synthesis is not matrix (e.g. DNA or RNA) driven, but results from a co- and posttranslational modification of glycoproteins and glycolipids. Since melanoma cells are not differentiated in a full manner, their surface glycans are altered in the way, which allowed us to find few specific glycan markers on a surface of melanoma cells[37]. Glycan-binding proteins – lectins – were used in current work to target specific melanoma tissue by conjugations with nanocrystals.

The problem here is that only light of longer wavelengths (above 600 nm) can penetrate living tissues (saturated with water) deep enough to ensure efficient visualization of all possible tumor nodes. Thus, practical markers should be activated/detected keeping this in mind as the main priority. One of candidates are Eu^{3+} ions with the emission at 610 and much less explored emission at 690 nm, both within the preferable spectral range. Therefore, in this paper, complementary results obtained for ultrasmall and brightly luminescent $NaGdF_4:Eu^{3+}$ nanocrystals are presented. What is more, the authors of this work illustrate in detailed manner how optical properties of such nanocrystals can be tuned and provide an example of their use as markers for melanoma cancer imaging probes.

2 Experimental section

2.1 Optical Equipment

Fluorescent microscopy was performed with fixed slides under a Carl Zeiss AxioImager A1 DIC/fluorescent microscope (Oberkochen, Germany) using 0.4NA 10x, 0.75 NA 40× air and 1.3 NA 100× oil immersion objectives. Fluorescent images were taken by a Zeiss AxioCam MRmIII cooled digital CCD camera under constant exposure. Fluorescence of NCs was evaluated at red channel (610 nm emission was obtained at 532 nm excitation) and at similar conditions the emission at near-IR channel (700 nm) was detected. H&E images were made at the same microscope set up using additional Canon (Japan) CCD RGB camera with constant focus and exposure settings. Image analysis was performed using Fiji software. Low-resolution photoluminescence (PL) and PL excitation spectra have been obtained at excitation from 450 W Xenon lamp coupled to monochromator (Triax 180, Horiba JY) and detected with HR400 Ocean Optics spectrometer. High resolution PL spectrum has been recorded by CCD camera (Synapse, Horiba JY) coupled to monochromator (Triax 550, Horiba JY) at excitation with 405 laser diode.

The time-resolved photoluminescence (PL) spectra and PL decay times were measured using modified QuantaMaster system from Photon Technology International (PTI). An Nd^{3+}:YAG laser equipped with Optical Parametric Resonator (Opolette from OPOTEK Inc.) has been used as the pulsed excitation source. For Maximum Entropy Analysis we used commercially available software (PTI).

2.2 Nanocrystals growth

Depending of the desired nanocrystal architecture three different synthesis methods were used to synthesize hydrophobic $NaGdF_4:Eu^{3+}$ NCs of various size. The trioctylphosphine oxide (TOPO) capped NCs, which after surface functionalization were used as markers, have been prepared by

modified co-thermolysis method which in details we described elsewhere[38]. The synthesis of NCs with various Eu^{3+} ions doping were conducted in oleic acid (OA) and octadecene (ODE) as a coordinating and noncoordinating solvents, respectively[39]. The reference sample of the big NCs (diameter > 50 nm) was prepared according to the literature method[40].

2.3 Nanocrystals transfer to water

NCs functionalization to hydrophilic $NaGdF_4:Eu^{3+}$-COOH form has been obtained according to our variant of Ligand Exchange method, which is patent pending (application number P408279). Typically, to NC solution in toluene we added another solution containing hydrophilic ligand and mixed them for some time under inert conditions. In particular, we substituted trioctylphosphine oxide (TOPO) or oleic acid (OA) with meso-2,3-dimercaptosuccinic acid (DMSA), which resulted in water dispersible NCs with carboxylic (COOH) groups on their surface.

2.4 Nanocrystals bio-conjugation

$NaGdF_4:Eu^{3+}$-COOH were sonicated and filtered through 0.22µm pore filter, then transferred to MES 0.1M pH 4,5 buffer. Lectin to be used for conjugation was dissolved in MES, 0.1M, pH 4,5 at 10 mg/ml. 2mg of protein were added to every 1ml of NC suspension (containing 10mg of NC). EDC (1-ethyl-3-(3-dimethylaminopropyl) carbodiimide hydrochloride) was added to reaction medium to obtain final 2% concentration. Suspension was reacted for 2h at room temperature under constant mixing. Obtained suspension was dialyzed against PBS 3 times to remove low molecular weight compounds, then lectin- $NaGdF_4:Eu^{3+}$ conjugates were purified from unbound protein by centrifugation with Amicon 100kDA cut-off filter. For purposes BSA (1% final concentration) and sodium azide

(0.05% final concentration) were added to NC suspension. Narcissus poeticus lectin (NPL) and peanut agglutinin (PNA) lectins were used to visualise undifferentiated melanoblasts developed between blood vessel and areas of necrosis and differentiated melanin-producing melanoblasts, correspondingly as described by us previously for mouse B16F10 melanoma[37].

2.5 Melanoma tumor growth and induction

The C57BL/6 mouse-derived B16F10 melanoma cell line was propagated in a DMEM supplemented with 10% fetal bovine serum (FBS) and penicillin/streptomycin and were re-seeded every 3 to 5 days, so that a confluent layer is not formed. Cells were grown in culture dishes, detached from cell surface with trypsin/EDTA, washed in DMEM w/o serum and centrifuged. Cell pellet was resuspended at 40 million cells/ml and 100µl of cell suspension (containing in total 4 million of cells) was injected subcutaneously into the back region of C57BL/6 mice[41]. C57BL/6 mice were bred at Danylo Halytsky Lviv National Medical University, Lviv, Ukraine and kept on a standard diet with food and water available ad libitum. Animal hair was trimmed at the place of injection and tumor growth was monitored with calliper every 3 days. Animal studies were conducted according to European principles and guidelines for the care and use of laboratory animals and were approved by Ethical Council of DH LNMU, approval 20130624/6.

2.6 Preparation of histological slides.

Mice were sacrificed with cervical dislocation under dimethyl ether anaesthesia. The tumors were removed, if needed (depending on tumor size) sliced centromedially and fixed overnight in 4% neutral buffered formalin, then embedded in paraffin wax according to the standard protocol. Obtained formalin fixed paraffin-embedded (FFPE) tissue samples were used for histological analysis and for bioimaging. For general morphology studies, 5 to 7 µm thick sections were stained with haematoxylin and eosin (H&E), for discrimination of capillary networks Delafield haematoxylin with eosin were used. For fluorescent microscopy, slides were counterstained with DAPI if needed.

2.7 Bioimaging

Ex vivo tracking of formalin-fixed tissue samples was performed with a Bruker Xtreme in Vivo machine supplied with interline front-illuminated (FI) 16 MP CCD detector, 400 W Xenon Fluorescence illuminator (excitation wavelength range: 410 nm – 760 nm, emission filter wavelength range: 535 nm – 830 nm) and module for animal warming air 20°C– 40°C as described by us earlier[42]. The data was analysed by high-performance Bruker Molecular Imaging (MI) software.

3 Results

3.1 Structural properties

Figure 1a shows example of TEM image of smallest β-$NaGdF_4$:Eu^{3+} nanocrystals obtained by us. As it can be seen from this image, these hydrophobic nanocrystals can be grown as small as 3-5 nm in size as well as big with size of up to around 50 nm (Figure 1b). In both cases however, they have plate-like shape with hexagonal structure, what is clearly seen in inset in Figure 1b. These nanocrystals can be further covered with $NaGdF_4$ shell. Obtaining efficient shell increase the nanocrystals size about twice, making their size distribution slightly wider (Figure 1d, e) but improving their optical properties what will be discussed in more details in next paragraphs.

3.2 Optical properties

The excitation and emission spectra of Eu^{3+} ions are characterized by a series of narrow lines related mainly to f-f intra-shell transitions. However, the spectra can be slightly modified by using the surface chemistry[43] or ions co-doping[44,45]. The emission properties of nanocrystals obtained by us can be tuned by changing Eu^{3+} concentration[43] and co-doping i.e. with Tb^{3+} ions[44]. This has been shown in Figure 2a. In the limit case, the emission of β-$NaEuF_4$ nanocrystals is concentrated at 610 and 720 nm lines.

These emission wavelengths are very promising from the application point view since both are located in the biological window (600-800 nm[46]) with the minimum absorption at 700 nm. Especially moving from 500 nm up to 700 nm reducing the absorption of melanosome interior by almost an order of magnitude[46]. Another consequence of moving from 500 nm into the red-infrared spectral range is the reduction of light scattering, which is very high for skin when compared to other tissues[46]. Thus, emission at 610 and 720 nm seems to be very promising for optical imaging.

The price we have to pay for having a high emission intensity (quantum yield – QY – around 30-50%) as compared to up-converting nanocrystals (i.e. β-$NaYF_4$:Er^{3+}, Yb^{3+} with typical quantum yield in the order of ~0,35%[47]) is excitation in the visible spectral range with 532, 465, 395 nm or even with the wavelengths more in UV. For these wavelengths, the scattering and absorption/autofluorescence of the tissue are much higher as compared with 980 nm wavelength excitation. On the other hand, the emission in this case is significantly stronger when comparing QY for both types of NCs. Thus, the final comparison of these two markers is very difficult and depends on number of factors like tissue thickness, contamination of water, blood, oxygen etc.

Nevertheless, we can control slightly the excitation profile of europium-doped fluorides by small modifications of its matrix what has been shown in Figure 2b. The main mechanism enabling to do this is ion-ion interactions and energy/charge transfer between different energy levels introduced into nanocrystals by other ions or surface ligands (Figure 2c). In particular, the reference sample (doped with 1% of Eu^{3+} ions and 50 nm in size) has the least complicated spectrum (few energy levels visible). Increasing the concentration of the dopant (here to 100%) one can induce charge transfer (CT)

states, whereas co-doping whit other lanthanides results in energy transfer and different color emission.

From Figure 2b it is visible that $NaGdF_4:Eu^{3+}$ NCs can be easily excited in UV when Tb^{3+} or Gd^{3+} ions are introduced or charge transfer states related with the surface ligands (i.e. TOPO, OA) are involved. One typical feature for nanocrystals doped with lanthanides is the presence of two different ions sites in their crystal lattice, which are surface and volume site. These two sites characterize with slightly different excitation, emission and relaxation properties[43]. Thus, to homogenize these properties a several approaches can be used. Figure 3d shows the emission decay time measured at 610 nm for two nanocrystals with a different Eu^{3+} concentration: 1 and 100% ($NaEuF_4$). In both cases, two components of the emission decay, related with these two different Eu^{3+} sites can be clearly observed while for $NaEuF_4$ sample this effect is much more visible because statistically more Eu^{3+} ions are placed at the nanocrystals surface. One of the possible ways to remove the fast component (surface Eu^{3+} related) is to make core-shell structures. Results obtained for this approach for both concentrations are shown in Figure 3b. In addition to reduction of fast component in both cases, for nanocrystals with low Eu^{3+} concentration the emission rise time increases significantly indicating absence of ion-ion interactions within the nanocrystals volume. This is due to slight ions diffusion to outer, undoped shell layer increasing average distance between Eu^{3+} ions.

The other way we have used to reduce the fast component of the emission decay is more statistical approach and Figure 3c shows the reduction of the fast component by simply increasing the size of nanocrystals from around 5 up to 50 nm. This increase in size reduces the surface-to-volume ratio lowering the number of surface Eu^{3+} ions, which diminishes the contribution of fast component of resultant emission decay times. This works mainly for nanocrystals doped with low Eu^{3+} concentrations where fast component is completely reduced. Therefore, precise control of nanocrystals' size and architecture as well as ion-ion interactions enables us to select the best ones for specific application and imaging system capabilities. Thus, the optimal NCs' architecture is either small core-shell geometry or large core ones.

In next step, our nanocrystals have been transferred to water with ligand exchange protocol being content of a pending polish patent (P408279). Obtained in this way β-$NaGdF_4:Eu^{3+}$-COOH nanocrystals have been bio-conjugated with lectins NPL and PNA to target melanoma cells. Created nanocrystals have not demonstrated any significant cytotoxicity in cell cultures of HeLa (human epithelia) and B16F10 (human melanoma) cells and were used for injection into the bloodstream of mouse bearing syngeneic melanoma tumor. After 1 or 24 hours the tumor has been removed from the mice and analysed with a different imaging techniques. Schematically, this procedure has been shown in Figure 4a.

FFPE blocks were used to obtain histological sections stained by means of conventional histology to visualize melanoma tissue as well as counterstained with DAPI to visualize cell nuclei and image in fluorescence mode to visualize injected conjugates of nanocrystals.

3.3 Optical imaging

Obtained histological slides were imaged by fluorescence microscopy using standard filter sets used to visualize red (emission 610 nm) or NIR labels (emission 690 nm). β-$NaGdF_4:Eu^{3+}$ NCs conjugated with PNA lectin targeting melanin-producing cells have produced a strong Eu-related fluorescence, which was easily overcoming light-absorbing properties of black melanin tissue. Besides, projections of melanoma tissue, usually not visualized by melanin and dispersed cells (those to be usually ignored/neglected by surgeons) were well seen in fluorescent mode with red fluorescence (Figure 5).

To test photostability of the developed NCs, tissue stained with NPL-lectin conjugated β-$NaGdF_4:Eu^{3+}$ NCs and targeting melanoma tissues around blood were subjected to continuous excitation with 100 Watt HBO Hg lamp with 546±12 nm excitation filter for 15 minutes. Fluorescent emission detected with 610±60 nm filter was measured for specific and nonspecific areas and signal-to-noise ratio (S/N) was calculated. Unlike many other organic dyes, signal intensity of NCs was stable over the whole length of irradiation. Moreover, since autofluorescence signal bleached with time, the S/N increased in course of continuous irradiation. This demonstrated that developed optical probes possess high photostability, which is important for constant monitoring, e.g. during surgical operation on tumor removal (Figure 6).

On the next step, we used formalin-fixed melanoma tissue sample to provide ex vivo imaging in order to evaluate the possibilities of melanoma tissue detection in the organism and compare different excitation/emission rates used for tissue imaging. Testing of melanoma tissues samples obtained from mice after injection of NPL-β-$NaGdF_4:Eu^{3+}$ and PNA-β-$NaGdF_4:Eu^{3+}$ 1 hour and 24 hours before removing the tumors from the body revealed effective tumor visualization when using 530 nm excitation and 600 nm emission channel with signal intensity of 118 pW/cm^2 and 530 nm excitation and 700 nm emission channel with signal intensity of 78118 pW/cm2 (Figure 7a, b).

Parts of tumor providing high signal of NCs were subjected to histological analysis and revealed abundant vascularization and presence of melanocytes, thus indicating the effectiveness of their labelling with created lectin-conjugated NCs. Fluorescence intensity of tumor samples was estimated by analysing emission at 610 and 700nm and using the excitation by distinct wavelengths in the range of 450-620 nm. Obtained data (Figure 7e) indicate the good correspondence of emission intensity depending on the excitation spectra of β-$NaGdF_4:Eu^{3+}$ NCs.

3 Conclusions

Here the authors describe the β-$NaGdF_4:Eu^{3+}$ nanocrystals, which possess high brightness and photostability. The bio-functionalization and bio-targeting strategies of the

aforementioned NCs are presented as well as the ability of created conjugates to reach targeted tissue after injection in the bloodstream of experimental animals. NC-targeted mouse melanoma tissue was effectively visualized by fluorescent microscopy in histological slices and ex vivo in fixed melanoma tumors. These properties make NCs a good candidate for visualization probes during detection of superficially located tumors and pathological tissue.

Acknowledgements

The authors are grateful to West-Ukrainian BioMedical Research Center. This work was supported by the grants from the Polish National Science Centre, Sonata Bis 3 Project No. UMO-2013/10/E/ST5/00651. We thank Prof. M. Herrmann and Dr. L. Munoz for providing specific B16F10 cell lines; Dr. N. Prevarskaya, Dr. V. Lehen'kyi and P. Mariot, Laboratoire de Physiologie Cellulaire INSERM U1003, Contre le Cancer et LABEX (Laboratoire d'excellence), Universit´ e Lille1 for their help in ex vivo imaging of melanoma tissue samples; Dr. S. Vari and RECOOP HST Association for their help in organizing current research project, Prof. R. Stoika for reading and editing the paper.

Notes and references

1 S. Kim, Y. T. Lim, E. G. Soltesz, A. M. De Grand, J. Lee, A. Nakayama, J. A. Parker, T. Mihaljevic, R. G. Laurence, D. M. Dor, L. H. Cohn, M. G. Bawendi and J. V. Frangioni, *Nat. Biotechnol.*, 2004, **22**, 93–97.
2 A. M. Derfus, W. C. W. Chan and S. N. Bhatia, *Nano Lett.*, 2004, **4**, 11–18.
3 J. Hu, L. Li, W. Yang, L. Manna, L. Wang and A. P. Alivisatos, *Science*, 2001, **292**, 2060–2063.
4 L. Sudheendra, G. K. Das, C. Li, D. Stark, J. Cena, S. Cherry and I. M. Kennedy, *Chem. Mater.*, 2014, **26**, 1881–1888.
5 C. Liu, Z. Gao, J. Zeng, Y. Hou, F. Fang, Y. Li, R. Qiao, L. Shen, H. Lei, W. Yang and M. Gao, *ACS Nano*, 2013, **7**, 7227–7240.
6 Y. Dai, P. Ma, Z. Cheng, X. Kang, X. Zhang, Z. Hou, C. Li, D. Yang, X. Zhai and J. Lin, *ACS Nano*, 2012, **6**, 3327–3338.
7 G. Tian, Z. Gu, L. Zhou, W. Yin, X. Liu, L. Yan, S. Jin, W. Ren, G. Xing, S. Li and Y. Zhao, *Adv. Mater.*, 2012, **24**, 1226–1231.
8 Z. Liu, Z. Li, J. Liu, S. Gu, Q. Yuan, J. Ren and X. Qu, *Biomaterials*, 2012, **33**, 6748–6757.
9 H. Xing, W. Bu, S. Zhang, X. Zheng, M. Li, F. Chen, Q. He, L. Zhou, W. Peng, Y. Hua and J. Shi, *Biomaterials*, 2012, **33**, 1079–1089.
10 T. Yang, Y. Sun, Q. Liu, W. Feng, P. Yang and F. Li, *Biomaterials*, 2012, **33**, 3733–3742.
11 X. Zhu, J. Zhou, M. Chen, M. Shi, W. Feng and F. Li, *Biomaterials*, 2012, **33**, 4618–4627.
12 J. Liu, W. Bu, L. Pan, S. Zhang, F. Chen, L. Zhou, K. Zhao, W. Peng and J. Shi, *Biomaterials*, 2012, **33**, 7282–7290.
13 S. Zeng, M.-K. Tsang, C.-F. Chan, K.-L. Wong and J. Hao, *Biomaterials*, 2012, **33**, 9232–9238.
14 L. Zeng, L. Xiang, W. Ren, J. Zheng, T. Li, B. Chen, J. Zhang, C. Mao, A. Li and A. Wu, *RSC Adv.*, 2013, **3**, 13915–13925.
15 R. Bilyy and A. Podhorodecki, *Nanomed.*, 2015, **10**, 1997–2000.
16 L. Xiong, T. Yang, Y. Yang, C. Xu and F. Li, *Biomaterials*, 2010, **31**, 7078–7085.
17 J.-C. Zhou, Z.-L. Yang, W. Dong, R.-J. Tang, L.-D. Sun and C.-H. Yan, *Biomaterials*, 2011, **32**, 9059–9067.
18 B. Sojka, M. Kuricova, A. Liskova, M. Bartusova, M. Banski, J. Misiewicz, M. Dusinska, M. Horvathova, E. Jahnova, S. Ilavska, M. Szabova, E. Rollerova, A. Podhorodecki and J. Tulinska, *J. Appl. Toxicol. JAT*, 2014, **34**, 1220–1225.
19 S. Wu, G. Han, D. J. Milliron, S. Aloni, V. Altoe, D. V. Talapin, B. E. Cohen and P. J. Schuck, *Proc. Natl. Acad. Sci.*, 2009, **106**, 10917–10921.
20 Y. Sun, X. Zhu, J. Peng and F. Li, *ACS Nano*, 2013, **7**, 11290–11300.
21 X. Teng, Y. Zhu, W. Wei, S. Wang, J. Huang, R. Naccache, W. Hu, A. I. Y. Tok, Y. Han, Q. Zhang, Q. Fan, W. Huang, J. A. Capobianco and L. Huang, *J. Am. Chem. Soc.*, 2012, **134**, 8340–8343.
22 Z. Li and Y. Zhang, *Nanoscale*, 2010, **2**, 1240–1243.
23 F. Wang, R. Deng, J. Wang, Q. Wang, Y. Han, H. Zhu, X. Chen and X. Liu, *Nat. Mater.*, 2011, **10**, 968–973.
24 A. Podhorodecki, A. Noculak, M. Banski, B. Sojka, A. Zelazo, J. Misiewicz, J. Cichos, M. Karbowiak, B. Zasonska, D. Horak, B. Sikora, D. Elbaum, T. Dumych, R. Bilyy and M. Szewczyk, *ECS Trans.*, 2014, **61**, 115–125.
25 J. Ma, P. Huang, M. He, L. Pan, Z. Zhou, L. Feng, G. Gao and D. Cui, *J. Phys. Chem. B*, 2012, **116**, 14062–14070.
26 J.-W. Shen, C.-X. Yang, L.-X. Dong, H.-R. Sun, K. Gao and X.-P. Yan, *Anal. Chem.*, 2013, **85**, 12166–12172.
27 G. Zhang, Y. Liu, Q. Yuan, C. Zong, J. Liu and L. Lu, *Nanoscale*, 2011, **3**, 4365–4371.
28 G. Chen, H. Qiu, P. N. Prasad and X. Chen, *Chem. Rev.*, 2014, **114**, 5161–5214.
29 Y. Min, J. Li, F. Liu, P. Padmanabhan, E. K. L. Yeow and B. Xing, *Nanomaterials*, 2014, **4**, 129–154.
30 D. Ni, J. Zhang, W. Bu, H. Xing, F. Han, Q. Xiao, Z. Yao, F. Chen, Q. He, J. Liu, S. Zhang, W. Fan, L. Zhou, W. Peng and J. Shi, *ACS Nano*, 2014, **8**, 1231–1242.
31 Q. Liu, Y. Sun, C. Li, J. Zhou, C. Li, T. Yang, X. Zhang, T. Yi, D. Wu and F. Li, *ACS Nano*, 2011, **5**, 3146–3157.
32 J. Peng, Y. Sun, L. Zhao, Y. Wu, W. Feng, Y. Gao and F. Li, *Biomaterials*, 2013, **34**, 9535–9544.
33 M. Longmire, P. L. Choyke and H. Kobayashi, *Nanomed.*, 2008, **3**, 703–717.
34 A. Piris and M. C. Mihm, *Hematol. Oncol. Clin. North Am.*, 2009, **23**, 467–480, viii.
35 E. Dean and P. Lorigan, *Expert Rev. Anticancer Ther.*, 2012, **12**, 1437–1448.
36 S. J. Ohsie, G. P. Sarantopoulos, A. J. Cochran and S. W. Binder, *J. Cutan. Pathol.*, 2008, **35**, 433–444.
37 T. Dumych, M. Lutsyk, M. Banski, A. Yashchenko, B. Sojka, R. Horbay, A. Lutsyk, R. Stoika, J. Misiewicz, A. Podhorodecki and R. Bilyy, *Croat. Med. J.*, 2014, **55**, 186–194.
38 M. Banski, A. Podhorodecki and J. Misiewicz, *Phys. Chem. Chem. Phys. PCCP*, 2013, **15**, 19232–19241.
39 A. D. Ostrowski, E. M. Chan, D. J. Gargas, E. M. Katz, G. Han, P. J. Schuck, D. J. Milliron and B. E. Cohen, *ACS Nano*, 2012, **6**, 2686–2692.
40 J. Ryu, H.-Y. Park, K. Kim, H. Kim, J. H. Yoo, M. Kang, K. Im, R. Grailhe and R. Song, *J. Phys. Chem. C*, 2010, **114**, 21077–21082.
41 R. Chaurio, C. Janko, C. Schorn, C. Maueröder, R. Bilyy, U. Gaipl, G. Schett, C. Berens, B. Frey and L. E. Munoz, *Autoimmunity*, 2013, **46**, 317–322.
42 K. Turcheniuk, T. Dumych, R. Bilyy, V. Turcheniuk, J. Bouckaert, V. Vovk, V. Chopyak, V. Zaitsev, P. Mariot, N. Prevarskaya, R. Boukherroub and S. Szunerits, *RSC Adv.*, 2015, **6**, 1600–1610.

43 A. Podhorodecki, M. Banski, A. Noculak, B. Sojka, G. Pawlik and J. Misiewicz, *Nanoscale*, 2013, **5**, 429–436.
44 A. Podhorodecki, M. Banski, J. Misiewicz, M. Afzaal, P. O'Brien, D. Cha and X. Wang, *J. Mater. Chem.*, 2012, **22**, 5356–5361.
45 M. Banski, M. Afzaal, D. Cha, X. Wang, H. Tan, J. Misiewicz and A. Podhorodecki, *J. Mater. Chem. C*, 2014, **2**, 9911–9917.
46 S. L. Jacques, *Phys. Med. Biol.*, 2013, **58**, R37–61.
47 M. K. Stefan Wilhelm, *Nanoscale*, 2014, **7**.
48 "Optical Absorption of Hemoglobin," can be found under http://omlc.org/spectra/hemoglobin/
49 "The optical properties of pure water," can be found under http://omlc.org/spectra/water/abs/buiteveld94.html
50 R. L. P. van Veen, H. j. c. m. Sterenborg, A. Pifferi, A. Torricelli and R. Cubeddu, OSA, 2004, p. SF4.
51 K. F. Palmer and D. Williams, *J. Opt. Soc. Am.*, 1974, **64**, 1107.
52 R. M. Pope and E. S. Fry, *Appl. Opt.*, 1997, **36**, 8710.

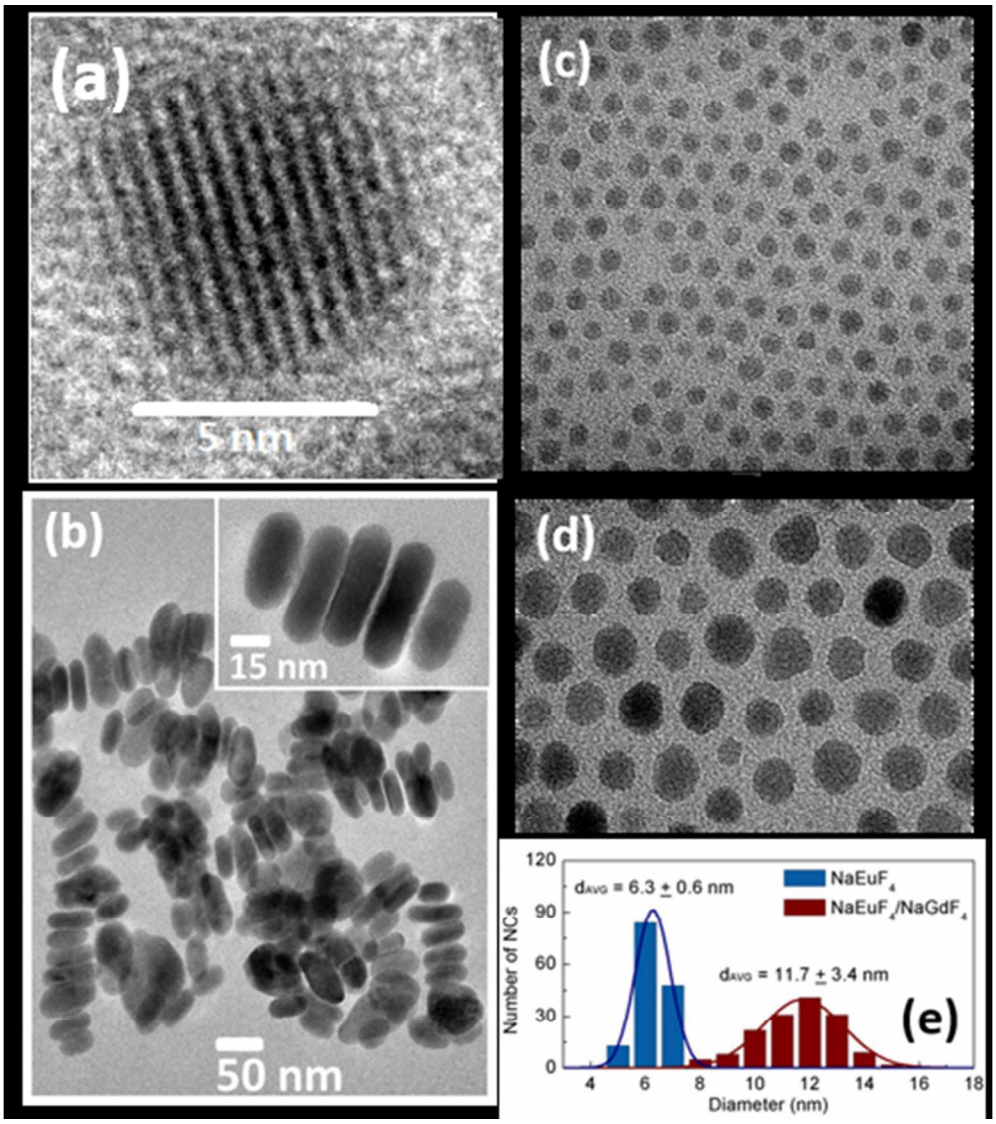

Figure 1. HRTEM image (a) of small (~6-7 nm) β-$NaGdF_4$:Eu^{3+} nanocrystals, (b) big (~50 nm) β-$NaGdF_4$:Eu^{3+} nanocrystals, (c) small (~6-7 nm) β-$NaGdF_4$:Eu^{3+} nanocrystals (d) covered with $NaGdF_4$ shell, (e) size distributions of core β-$NaEuF_4$ and core-shell β-$NaEuF_4$/$NaGdF_4$ nanocrystals
83x94mm (150 x 150 DPI)

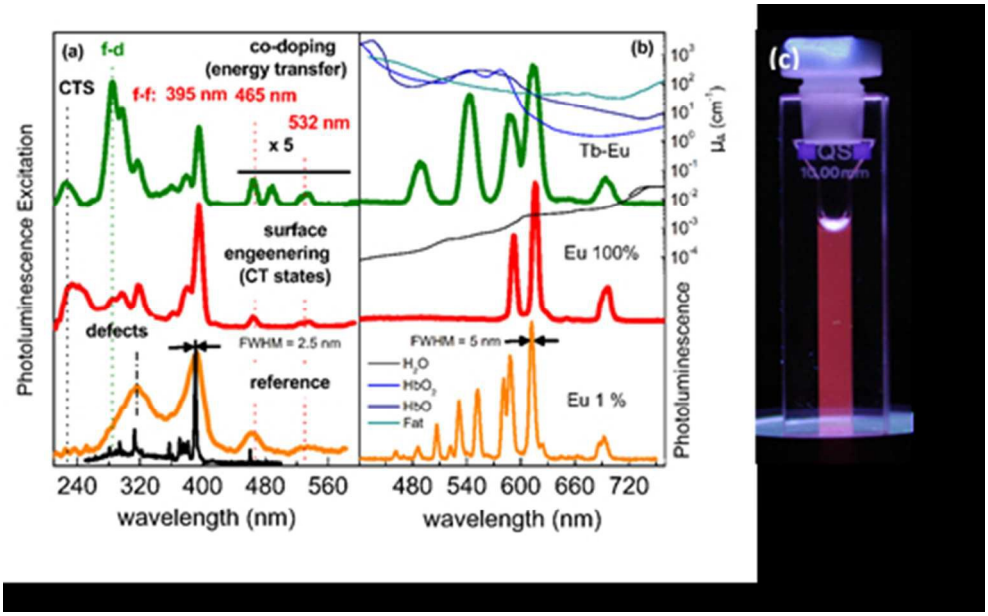

Figure 2. Optical properties of β-$NaGdF_4$:Eu^{3+} nanocrystals. (a) Excitation and (b) emission spectra recorded at 610 nm for β-$NaGdF_4$:Eu^{3+}, Tb^{3+}, β-$NaEuF_4$ and β-$NaGdF_4$:Eu^{3+} (1%). (c) Digital image recorded for β-$NaEuF_4$ sample at 395 nm excitation wavelength. Figure 2(a) includes exemplary high-resolution excitation spectrum obtained for β-$NaGdF_4$:Eu^{3+} (1%) NCs to demonstrate the importance of experimental conditions to make conclusions regarding optical properties of markers. In addition, Figure 2(b) shows absorption coefficient (μ_A) spectra of pure water, haemoglobin and fat taken from references [48–52]
82x51mm (150 x 150 DPI)

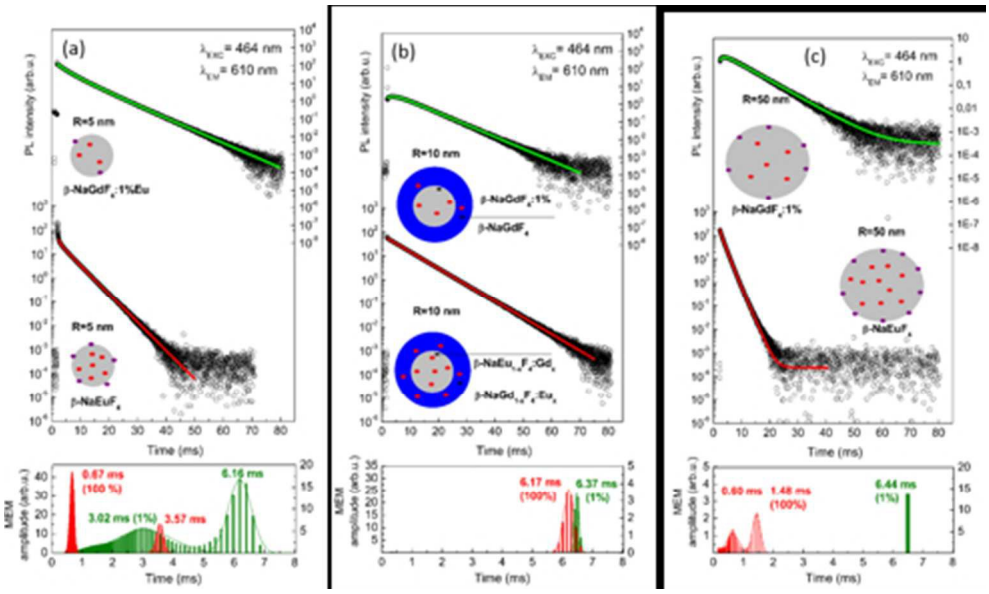

Figure 3. Temporal properties of β-$NaGdF_4$:Eu^{3+} nanocrystals. (a) 5 nm β-$NaEuF_4$ and β-$NaGdF_4$:Eu^{3+} 1%, (b) 5 nm β-$NaEuF_4$/$NaGdF_4$ and β-$NaGdF_4$:Eu^{3+} 1%/$NaGdF_4$, (c) 50 nm β-$NaEuF_4$ and β-$NaGdF_4$:Eu^{3+} 1%
82x49mm (150 x 150 DPI)

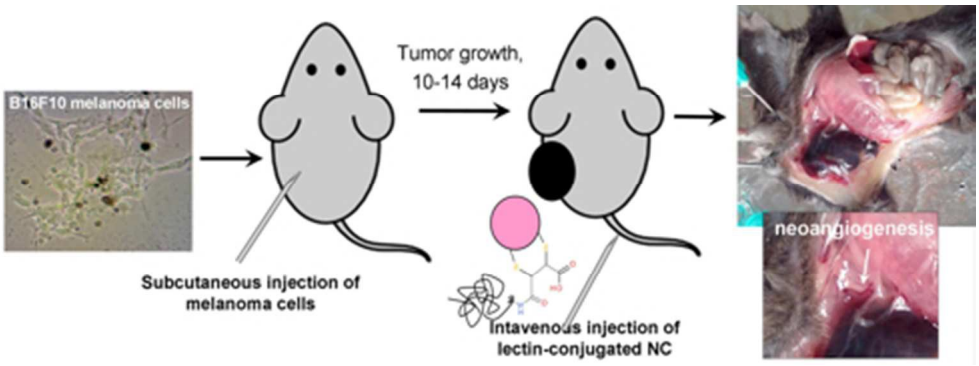

Figure 4. Principle of in vivo labelling of melanoma with lectin-conjugated β-$NaGdF_4$:Eu^{3+}-CO-NH-lectin nanocrystals. Melanoma is characterized by abundant angiogenesis, thus intravenous injection into tail vein was used to deliver lectin-conjugated NCs
82x30mm (150 x 150 DPI)

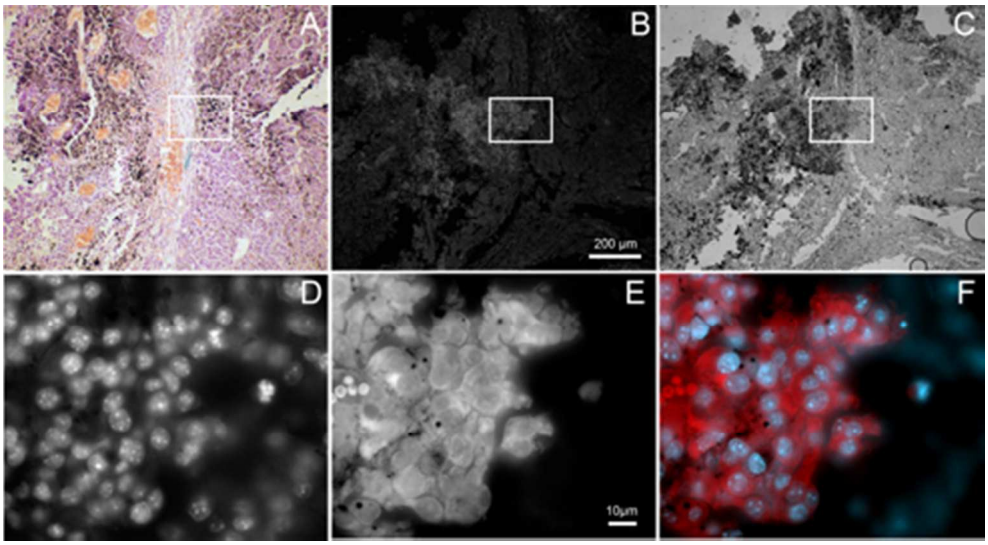

Figure 5. Visualization of melanoma tissue with PNA-conjugated β-$NaGdF_4$:Eu^{3+} NCs. Mouse melanoma tissue was stained by H&E (A) demonstrating abundant vessels (orange) and sites of melanin production (black) the sequential tissue slice was visualized for red fluorescence (ex. 546/12 nm, em. 610/60nm); the same field of view imaged in bright field mode demonstrated the light absorbance of melanin. D-F represent high magnification of the indicated region, with fluorescence of DAPI to counterstain nuclei (D), β-$NaGdF_4$:Eu^{3+} NCs (E) and merged signal (F)
82x45mm (150 x 150 DPI)

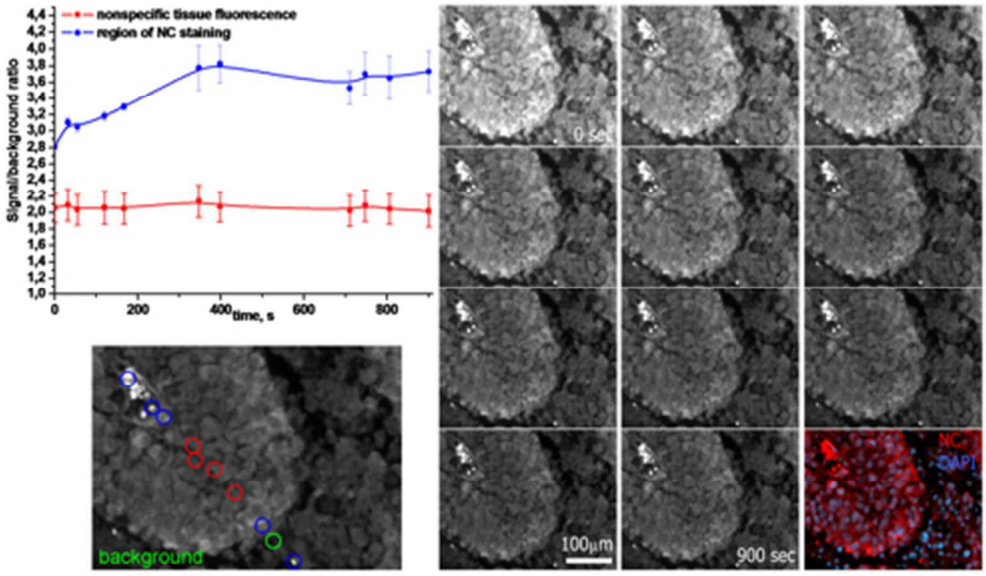

Figure 6. Samples stained with NPL-β-$NaGdF_4$:Eu^{3+} NCs targeting tumor tissue around blood vessels was continuously irradiated with 546±12 nm light and red fluorescence was detected. Fluorescence intensity of specific and nonspecific staining regions was measured in the indicated places over 900 seconds (left) and S/N ration was calculated. The panel at right represents sequential imaging of melanoma tissue during the course of irradiation. Last insert demonstrates merged image with nuclei counterstained with DAPI
82x48mm (150 x 150 DPI)

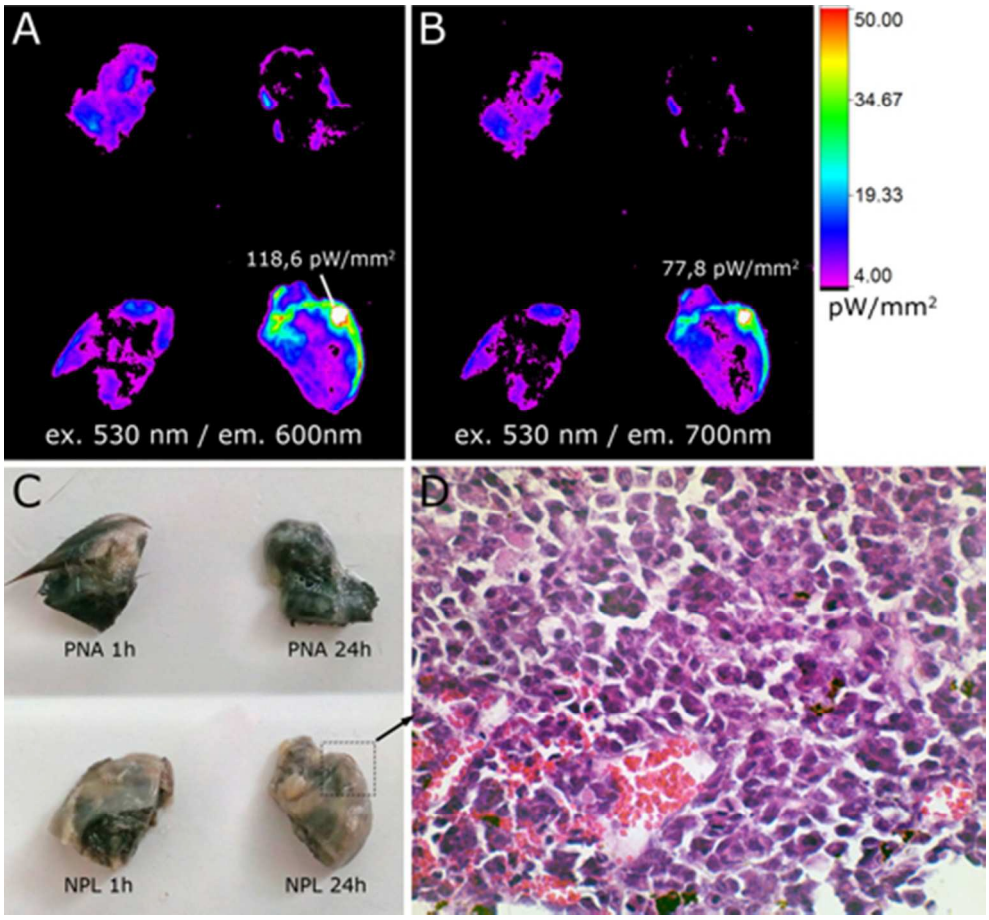

Figure 7. Ex vivo imaging of fixed melanoma samples after injection of NPL and PNA lectin-conjugated NCs into mice blood stream and post-treatment of animal for 1 and 24 hours. A, B – fluorescence of Eu^{3+} crystals using 530 nm excitation and 600 or 700 nm emission correspondingly. C – Light images of tumors indicating the area of tissue further subjected to histological analysis (D)
82x76mm (150 x 150 DPI)